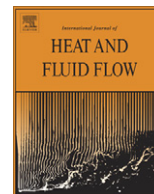


Contents lists available at [SciVerse ScienceDirect](http://www.sciencedirect.com)

International Journal of Heat and Fluid Flow

journal homepage: www.elsevier.com/locate/ijhff

Numerical simulation of compressible two-phase flow using a diffuse interface method

M.R. Ansari^{*}, A. Daramizadeh

Mechanical Engineering Department, Tarbiat Modares University, P.O. Box 14115-143, Tehran, Islamic Republic of Iran

ARTICLE INFO

Article history:

Received 14 March 2012
 Received in revised form 7 January 2013
 Accepted 11 February 2013
 Available online xxxx

Keywords:

Compressible multiphase flow
 Shock waves
 Cavitations
 Interfacial instability
 Godunov method

ABSTRACT

In this article, a high-resolution diffuse interface method is investigated for simulation of compressible two-phase gas–gas and gas–liquid flows, both in the presence of shock wave and in flows with strong rarefaction waves similar to cavitations. A Godunov method and HLLC Riemann solver is used for discretization of the Kapila five-equation model and a modified Schmidt equation of state (EOS) is used to simulate the cavitation regions. This method is applied successfully to some one- and two-dimensional compressible two-phase flows with interface conditions that contain shock wave and cavitations. The numerical results obtained in this attempt exhibit very good agreement with experimental results, as well as previous numerical results presented by other researchers based on other numerical methods. In particular, the algorithm can capture the complex flow features of transient shocks, such as the material discontinuities and interfacial instabilities, without any oscillation and additional diffusion. Numerical examples show that the results of the method presented here compare well with other sophisticated modeling methods like adaptive mesh refinement (AMR) and local mesh refinement (LMR) for one- and two-dimensional problems.

© 2013 Elsevier Inc. All rights reserved.

1. Introduction

Numerical simulation of multiphase or multi-component flow is a challenging subject with many applications in industry and in modeling natural phenomena. For example, multiphase or multi-component flows are significant in the physics of explosion, astrophysics, supersonic combustion systems, the detonation of high energy material and shock wave treatment of cancer in the medical industry. The models and numerical simulations presented in recent literature present different levels of accuracy and complexity. In general, these types of methods can be separated into two categories by how each considers the interfaces:

1. Sharp interface method (SIM)
2. Diffuse interface method (DIM)

In the sharp interface methods, a special effort is made to find the right location of the interface and to treat the interface explicitly. This method includes: general types of Lagrangian methods (Shopov et al., 1990); Euler methods, including the level set and VOF approaches (Pilliod and Puckett, 2004; Sethian, 1996; Osher and Fedkiw, 2001; Hu et al., 2009) combined Euler–Lagrangian methods, including front tracking and front tracking with ghost

fluid approaches (Unverdi and Tryggvason, 1992; Terashima and Tryggvason, 2009, 2010), ALE¹ methods (Doneal et al., 2004; Anbarlooei and Mazaheri, 2009) and MMIT² methods (Quan and Schmidt, 2007). The main weaknesses of these methods are high complexity, high computational cost, long CPU time and failure in interface prediction when the phenomena has no beginning or initial state for the interface (Saurel and Le Metayer, 2001). It should be emphasized that the ability to dynamically create interfaces that are not present initially is very important for flows with cavitations. For complicated interface conditions, the above-mentioned methods exhibit numerical diffusion and high numerical inaccuracy. Additionally, it is difficult to develop them to higher spatial cases (2D or 3D). Recently Chang and Liou (2007) have developed a stratified flow model that is capable of modeling compressible gas–liquid flows. However, the implementation of their method is highly complex.

In the second group of numerical methods, DIM, the interface is modeled as a numerically diffused zone (area), which is similar to capturing a discontinuity in gas dynamics (Saurel and Le Metayer, 2001). In fact, it can be mentioned that this type of diffused interface is a kind of artificial diffusion that is created by numerical calculations. These methods are divided into two general categories: those based on the Euler equations and those based on multiphase equations. The works based on the Euler equations include (Johnsen

^{*} Corresponding author. Tel.: +98 21 8288 3363; fax: +98 21 8800 5040.
 E-mail address: mra_1330@modares.ac.ir (M.R. Ansari).

¹ Arbitrary Lagrangian–Eulerian.

² Moving mesh interface tracking.

and Colonius, 2006; Kawai and Terashima, 2010; Shyue, 1998, 2010). These methods are restricted to applications in simple physical models with simple state equations. These methods are inaccurate in estimating the internal energy and temperature at the interface. The other category of models is based on multiphase equations (Abgrall, 1996). The most complete model is the seven-equation model introduced by Saurel and Abgrall (1999). This model contains two velocities and two pressures and is efficient for problems where the difference of phase velocities is important. Application of this model can present challenges due to non-conservative terms in the momentum, energy and volume fraction advection equations. In this basis many effort has been spent for modeling with this model (Munkejord, 2010; Tokareva and Toro, 2010; Dumbser and Toro, 2010). Another convenient model for simulation is the single-velocity six-equation model. This model is obtained by assuming the velocity relaxation time to be zero and was first introduced by Kapila et al. (2001). This model shows good capability in simulating two-phase flow with an interface when validated by Saurel et al. (2009). Another model that is suitable for multiphase flow simulation is the reduced five-equation model, also known as the Kapila model (Kapila et al., 2001; Murrone and Guillard, 2005). There are two main problems in using this model. First, the mixture sound velocity at the interface has non-monotonic behavior. Second, the volume fraction equation has a non-conservative term (Saurel et al., 2009). This model consists of two mass conservation equations, one momentum conservation equation, one energy conservation equation in the conservative form and one volume fraction advection equation in the non-conservative form. Recently, efforts to propose a suitable numerical method for the five-equation model have increased (Kreeft et al., 2010; Qamar and Ahmed, 2009; Kokh and Lagoutière, 2010). Murrone et al. (2005) applied the reduced five-equation model for two-phase flow simulation. In their two-dimensional test cases, the velocities were low, and the shock wave interaction with the interface of the two-phase flow was not considered. Kreeft and et al. (2010) presented a new version of the five-equation Kapila model. Their model was well behaved for two-dimensional compressible gas–gas flows. However, the model behavior for a two-dimensional gas–liquid interface was not demonstrated. Deledicque and Papalexandris (2007) suggested a conservative approximation for the five-equation model. This method is suitable for modeling of two-pressure solid–gas models or two phases with big differences in the material properties. This model has limited application and can only be used for two-phase solid–gas flow. Saurel et al. used the five-equation model in several recent studies (Petitpas et al., 2007, 2009; Saurel et al., 2007). In these studies, a new method and a new theory are added to the model based on shock wave relationships. In fact, their method is based on the development of a relaxation-projection method for the Euler equations. The projection method is an indirect method for differentiation of the advection equation. This method is more efficient than previous methods, but it is more difficult to implement and extend to unstructured grids. The main objective of the present work is to accurately simulate two-phase gas–gas and gas–liquid interfacial problems, as well as cavitation flow problems, with less computational cost by using reduced five-equation models. In this study, the HLLC Riemann solver is used for numerical simulation of compressible two-phase flow. To circumvent the inherent difficulties in solving the five-equation models outlined earlier, the following four steps were taken:

- Using appropriate sound velocity with less non-monotonic behavior, the wood sound relation is not applicable.
- A suitable discretization of the advection equation.
- Preventing negative pressure during numerical calculation of cavitation zones due to strong rarefaction waves reflecting from free surfaces by adapting a suitable cavitation equation of state.

- Numerical simulation of the governing equations using the Godunov numerical method and the HLLC solver.

In this article, the mathematical properties of the five-equation model and the Schmidt cavitation model are presented in Section 2. The numerical method is explained in detail in Section 3. The development of the model from the one- to two-dimensional case with second-order accuracy is presented in Sections 4 and 5. Finally, model verification and simulation results in one and two dimensions are presented in Section 6 and concluding remarks are presented in Section 7.

2. Kapila two-fluid flow model

The single speed, equal pressure, five-equation model is also known as the reduced five-equation, or Kapila, model. This model is the reduced model of Baer and Nunziato (1986). The multi-space governing equations of this model, with the exclusion of heat and mass transfer, are as follows:

$$\frac{\partial \alpha}{\partial t} + \vec{u} \cdot \vec{\nabla} \alpha = 0 \quad (1a)$$

$$\frac{\partial (\alpha_1 \rho_1)}{\partial t} + \nabla \cdot (\rho_1 \alpha_1 \vec{u}) = 0 \quad (1b)$$

$$\frac{\partial (\alpha_2 \rho_2)}{\partial t} + \nabla \cdot (\rho_2 \alpha_2 \vec{u}) = 0 \quad (1c)$$

$$\frac{\partial (\rho \vec{u})}{\partial t} + \nabla \cdot (\rho \vec{u} \otimes \vec{u}) + \vec{\nabla} P = 0 \quad (1d)$$

$$\frac{\partial (\rho E)}{\partial t} + \nabla \cdot ((\rho E + P) \vec{u}) = 0 \quad (1e)$$

where α , ρ , \vec{u} , P , E , e are the volume fraction, density, velocity vector, pressure, total energy and internal energy, respectively. The density is obtained from

$$\rho = (\alpha_1 \rho_1 + \alpha_2 \rho_2) \quad (2)$$

The two-phase mixture internal energy is calculated from

$$e = Y_1 \cdot e_1(\rho_1, P) + Y_2 \cdot e_2(\rho_2, P) \quad (3)$$

where

$$Y_k = \frac{(\alpha \rho)_k}{\rho} \quad (4)$$

where the subscript $k = 1, 2$ representing gas or liquid phase, respectively. In the present work, the stiffened-gas equation of state (SGS) is used. In the equal-pressure condition, the internal energy of phase, $e_k = e_k(\rho_k, P)$, is calculated using the following equation:

$$\forall k, \quad \rho_k e_k = \frac{P + \gamma_k \cdot P_{\infty, k}}{\gamma_k - 1} \quad (5)$$

where γ_k and $P_{\infty, k}$ are constant parameters of stiffend gas equation of state and are different for each fluid. The following equation for pressure is used to close the set of equations:

$$P(\rho, e, \alpha_k) = \frac{\rho e - \sum_k \frac{\alpha_k \gamma_k P_{\infty, k}}{\gamma_k - 1}}{\sum_k \frac{\alpha_k}{\gamma_k - 1}} \quad (6)$$

For this model the mixture sound velocity is defined as

$$c = \sqrt{\frac{\gamma \cdot (P + P_{\infty})}{\rho}} \quad (7)$$

$$\frac{1}{\gamma - 1} = \sum_k \frac{\alpha_k}{\gamma_k - 1}$$

$$\frac{\gamma \cdot P_{\infty}}{\gamma - 1} = \sum_k \frac{\alpha_k \gamma_k P_{\infty, k}}{\gamma_k - 1}$$

The Wood (1930) sound velocity $1/(\rho c_{eq}^2) = \alpha_1/(\rho_1 c_1^2) + \alpha_2/(\rho_2 c_2^2)$ has non-monotonic behavior at interface, which prevents correct shock wave transitions at the interface and leads to inaccurate calculation of dynamic acoustic waves. Saurel et al. (2009) proposed a frozen sound relationship, in which $c_{eq}^2 = Y_1 \cdot c_1^2 + Y_2 \cdot c_2^2$, to evaluate mixture sound velocity where the sound velocity has better monotonic behavior (higher effectiveness) in comparison to the Wood equation. But this sound relation has one main drawback. Even though the stiffened EOS (5) is not designed to properly represent the physics of strong reflecting rarefaction waves, such as cavitation zones. In some gas–liquid problems with strong rarefaction waves, pressure may drop to non-physical negative values that make the frozen sound relation unusable. The problem arises because it is not possible to apply the state equation for a perfect gas with a negative pressure, and the gas sound velocity becomes imaginary, resulting in computer code failure. For eliminating these difficulties in this paper, the modified Schmidt equation of state is used for regions with strong rarefaction waves and cavitations zones (Xie et al., 2006).

This method does not require partial differential equations and the pressure can be obtained analytically from the finite volume (computational cell) density, both of which reduce the computational cost. However, Schmidt (1997) proposed a constitutive relationship for the related saturated vapor and liquid in the cavitation zones based on the assumption of constant phase's sound speeds and constant phase densities. In this paper, the densities are updated in each time step.

In modified cavitation Schmidt model, a constant value was incorporated into the Schmidt model to prevent the pressure from becoming lower than the vapor pressure. This EOS is given as:

$$P = \begin{cases} SGEOS & P \geq P_{sat} \\ P_{sat} + P_{1-2} \cdot \log A & P_{\varepsilon} < P < P_{sat} \\ P_{\varepsilon} & P < P_{\varepsilon} \end{cases} \quad (8)$$

$$P_{1-2} = \frac{\rho_1 c_1^2 \rho_2 c_2^2 (\rho_1 - \rho_2)}{(\rho_1^2 c_1^2 - \rho_2^2 c_2^2)},$$

$$A = \frac{\rho_1 c_1^2 \rho_2 c_2^2 \cdot (\rho_2 + \alpha \cdot (\rho_1 - \rho_2))}{\rho_2 (\rho_1^2 c_1^2 - \alpha (\rho_1^2 c_1^2 - \rho_2^2 c_2^2))} \quad (9)$$

Following Xie et al. (2006), $P_{sat} = 2000$ Pa was assumed.

3. Numerical method

In this article, the Godunov numerical method was applied using the HLLC Riemann solver (Toro, 1999). In the one-dimensional case, the conservative part of the five-equation model can be written in the matrix form as:

$$U = \begin{bmatrix} \alpha_1 \rho_1 \\ \alpha_2 \rho_2 \\ \rho u \\ \rho E \end{bmatrix}, \quad \mathbf{f} = \begin{bmatrix} \alpha_1 \rho_1 u \\ \alpha_2 \rho_2 u \\ \rho u^2 + P \\ u(\rho E + P) \end{bmatrix} \quad (10)$$

$$\frac{\partial U}{\partial t} + \frac{\partial \mathbf{f}}{\partial x} = 0 \quad (11)$$

$$\frac{\partial \alpha}{\partial t} + u \frac{\partial \alpha}{\partial x} = 0 \quad (12)$$

Based on the Godunov numerical method, the discretization can be conducted as:

$$U_j^{n+1} = U_j^n - \frac{\Delta t}{\Delta x} \left[\mathbf{f}(U^*(u_j^n, u_{j+1}^n)) - \mathbf{f}(U^*(u_{j-1}^n, u_j^n)) \right] \quad (13)$$

The inter-cell flux of the HLLC Riemann solver has been presented by Toro (1999):

$$F_{j+\frac{1}{2}}^{HLLC} = \begin{cases} f(U_L) & 0 \leq S_L \\ f(U_L^*) = f(U_L) + S_L(U_L^* - U_L) & S_L \leq 0 \leq S^* \\ f(U_R^*) = f(U_R) + S_R(U_R^* - U_R) & S^* \leq 0 \leq S_R \\ f(U_R) & 0 \geq S_R \end{cases} \quad (14a)$$

$$U_k^* = \begin{bmatrix} \alpha_1 \rho_1 \frac{S_k - u_k}{S_k - S^*} \\ \alpha_2 \rho_2 \frac{S_k - u_k}{S_k - S^*} \\ \rho \frac{S_k - u_k}{S_k - S^*} S^* \\ \rho \frac{S_k - u_k}{S_k - S^*} [E_k + (S^* - u_k) \times \left[S^* + \frac{P_k}{\rho_k(S_k - u_k)} \right]] \end{bmatrix} \quad (14b)$$

where R and L are the right and left boundaries of cell, respectively. The waves that move to the right and the left are estimated by Davis (1998) method as:

$$S_R = \max(u_L + c_L, u_R + c_R), \quad S_L = \min(u_L - c_L, u_R - c_R) \quad (15)$$

The intermediate wave velocity is estimated by the HLL method:

$$S^* = \frac{(\rho u^2 + P)_L - (\rho u^2 + P)_R - S_L(\rho u)_L + S_R(\rho u)_R}{(\rho u)_L - (\rho u)_R - S_L \rho_L + S_R \rho_R} \quad (16)$$

The volume fraction is constant across the fluid trajectories, thus it changes only across S^* :

$$\alpha_{kR}^* = \alpha_{kR} \quad \alpha_{kL}^* = \alpha_{kL} \quad (17)$$

The non-conservative term at left side of the advection equation is $u \frac{\partial \alpha}{\partial x}$. For discretization of this term, the method presented by Saurel et al. (2009) was applied. First, the non-conservative term is rewritten as:

$$\vec{u} \cdot \vec{\nabla} \alpha = \text{div}(\alpha \cdot \vec{u}) - \alpha \cdot \text{div}(\vec{u}) \quad (18)$$

By substituting Eq. (18) in Eq. (1a), the advection equation in the one-dimensional case is written as:

$$\frac{\partial \alpha_1}{\partial t} + \frac{\partial (\alpha_1 u)}{\partial x} = (\alpha_1) \frac{\partial u}{\partial x} \quad (19)$$

The left side of this equation is in the conservative form. By using Godunov method for advection term, the discretized form of this equation becomes:

$$\alpha_{1j}^{n+1} = \alpha_{1j}^n - \frac{\Delta t}{\Delta x} \left[(u \alpha_1)_{j+\frac{1}{2}}^* - (u \alpha_1)_{j-\frac{1}{2}}^* - \alpha_{1j} \cdot (u_{j+\frac{1}{2}}^* - u_{j-\frac{1}{2}}^*) \right] \quad (20)$$

This form of discretization mostly guarantees a positive value for the volume fraction and increases the accuracy of the volume fraction calculation.

3.1. Solution procedure

The numerical method can be summarized as follows:

- At each cell boundary, solve the Riemann problem of System (1) with the HLLC solver of Section 4.
- Evolve all flow variables with the Godunov-type method.
- Compute the mixture pressure using Eq. (6).
- Evaluate the value of pressure (P). If the pressure is less than the physical saturated pressure (P_{sat}), then cavitation occurs and the pressure should be corrected by Eq. (8).
- Go to the first item for the next time step.

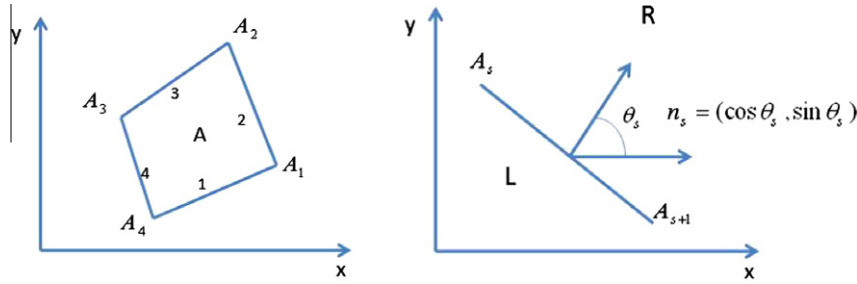


Fig. 1. Quadrilateral finite volume V in a two-dimensional domain in x - y space.

4. Upgrade to second-order spatial accuracy

To achieve the second-order spatial accuracy, the MUSCL method was used (Toro, 1999). This method is conducted in three steps, which include data reconstruction, evolution and solving of the Riemann problem.

– Data reconstruction

In this stage, the primitive variables on the cell boundary are extrapolated as:

$$W_{j+1/2}^- = W_j^n + \frac{1}{2} \delta j, \quad W_{j+1/2}^+ = W_j^n - \frac{1}{2} \delta j \quad (21)$$

The δj is function of $W_j^n - W_{j-1}^n, W_{j+1}^n + W_j^n$. Conducting this stage on the initial variables guarantees the uniformity of pressure and velocity. In this study, the Minmod limiter is applied.

– Evolution

In this stage, the $W_{j\pm 1/2}^\mp$ value is evaluated at a time step of $\frac{\Delta t}{2}$

$$\widehat{W}_{j+1/2}^+ = W_{j+1/2}^+ - \frac{\Delta t}{2\Delta x} A(W_j) (W_{j+1/2}^- - W_{j+1/2}^+), \quad (22)$$

$$\widehat{W}_{j+1/2}^- = W_{j+1/2}^- - \frac{\Delta t}{2\Delta x} A(W_j) (W_{j+1/2}^- - W_{j+1/2}^+)$$

– Riemann problem solution

In this stage, $\widehat{W}_{j\pm 1/2}^\mp$ is rewritten in the conservative form and the Riemann problem is solved.

5. Extension of the one-dimensional case to the two-dimensional case

A structured grid is used in the present work. However, modification of the one-dimensional case to a multi-dimensional case using the finite-volume technique is presented for both a structured and an unstructured mesh Toro (1999). A control volume V_i , with surface A and outward unit normal vector n is assumed as shown in Fig. 1. The integral form of the multi-space dimensional conservation laws are given below as Eq. (23):

$$\frac{d}{dt} \int_{V_i} U + \iint_A H \cdot n \cdot dA = 0 \quad (23)$$

In the two-dimensional case, the conservation variables vector is

$$U = ((\alpha\rho)_1, (\alpha\rho)_2, \rho u, \rho v, \rho E)$$

where $H = (F, G)$ is the flux tensor and is written as:

$$F = ((\alpha\rho)_1 u, (\alpha\rho)_2 u, \rho u^2 + P, \rho v u, (\rho E + P) u) \\ G = ((\alpha\rho)_1 v, (\alpha\rho)_2 v, \rho v u, \rho v^2 + P, (\rho E + P) v) \quad (24)$$

where $E = Y_1 e_1 + Y_2 e_2 + 0.5(u^2 + v^2)$ and $P = \alpha_1 P_1 + \alpha_2 P_2$.

The total flux through the boundaries is obtained from Eq. (23) and written as:

Table 1

Gas and liquid specifications and initial condition for the test case of interfacial movement in a flow with uniform pressure and velocity.

	$X < 0.5$ (m)		0.5 (m) $< X < 1$ (m)	
	Air	Water	Air	Water
ρ (kg/m ³)	10	1000	10	1000
u (m/s)	100	100	100	100
P (Pa)	10^5	10^5	10^5	10^5
α	10^{-6}	$1-10^{-6}$	$1-10^{-6}$	10^{-6}
P_∞ (Pa)	0	6e8	0	6e8
γ	1.4	4.4	1.4	4.4

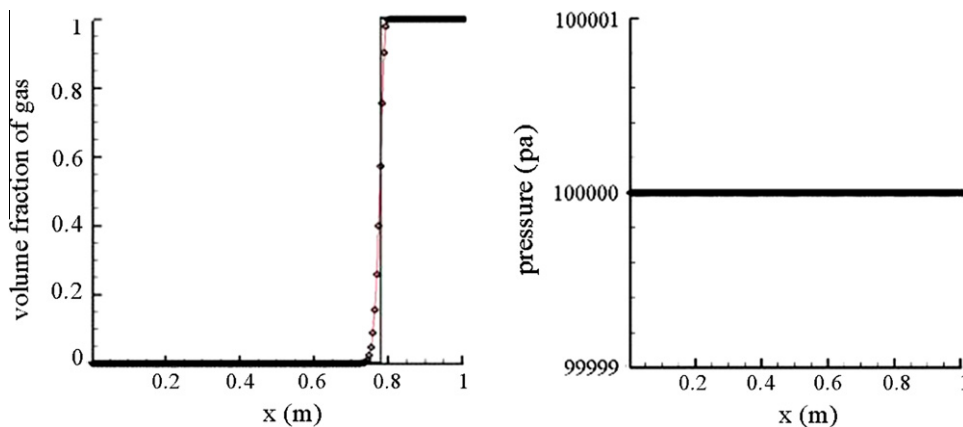


Fig. 2. Volume fraction and pressure profiles of a moving discontinuity problem, 200 computational cells, CFL = 0.8.

Table 2

Properties of air and water and the initial condition for shock tube of the air–water shock tube case.

	X < 0.7 (m)		0.7 (m) < X < 1 (m)	
	Air	Water	Air	Water
ρ (kg/m ³)	1	1000	1	1000
u (m/s)	0	0	0	0
P (Pa)	10 ⁹	10 ⁹	10 ⁵	10 ⁵
α	10 ^{−6}	1–10 ^{−6}	1–10 ^{−6}	10 ^{−6}
P_∞ (Pa)	0	6e8	0	6e8
γ	1.4	4.4	1.4	4.4

$$\iint_A H \cdot n \cdot dA = \sum_{s=1}^N \int_{A_s}^{A_{s+1}} H \cdot n_s \cdot dA \quad (25)$$

where s denotes the inter-cell boundary of $A_s A_{s+1}$. n_s can be calculated easily with respect to the θ_s angle.

$$n_s = (\cos \theta_s, \sin \theta_s) \quad (26)$$

In this case, the total transitional flux can be obtained from Eq. (27):

$$\sum_{s=1}^N \int_{A_s}^{A_{s+1}} H \cdot n_s \cdot dA = \sum_{s=1}^N \int_{A_s}^{A_{s+1}} [\cos \theta_s \cdot F(U) + \sin \theta_s \cdot G(U)] \cdot dA \quad (27)$$

The first integral term of Eq. (23) is the time rate of change of the mean of u in volume V , and it can be written as:

$$\frac{d}{dt} \iiint_V U \cdot dV = |V| \frac{d}{dt} U \quad (28)$$

After substitution and rearrangement:

$$\frac{d}{dt} U = -\frac{1}{|V|} \sum_{s=1}^N \int_{A_s}^{A_{s+1}} [\cos \theta_s \cdot F(U) + \sin \theta_s \cdot G(U)] \cdot dA \quad (29)$$

After time integration for the i th cell, the following calculation form is obtained:

$$U_i^{n+1} = U_i^n - \frac{\Delta t}{V_i} \sum_{s=1}^N L_s (F_s^* \cos \theta_s + G_s^* \sin \theta_s) \quad (30)$$

6. Test cases and code validation

The following standard test cases that include an interface were considered in this article:

- Interface movement in a flow with uniform pressure and velocity.
- Water–air shock tube.
- Interaction between a shock wave and a bubble in the two cases of:
 - Gas–gas phase (air–R22, air–helium)
 - Gas–liquid phase (air–water)
- Underwater explosion

6.1. Interface movement in a flow with uniform velocity and pressure

This case considers a volume fraction discontinuity movement (discontinuity in density) between two fluids at uniform atmospheric pressure and uniform movement velocity of 100 m/s. This discontinuity separates two pure fluids from each other. There is water, an almost pure fluid, on the left side and air on the right side. The initial condition and necessary fluid properties for this

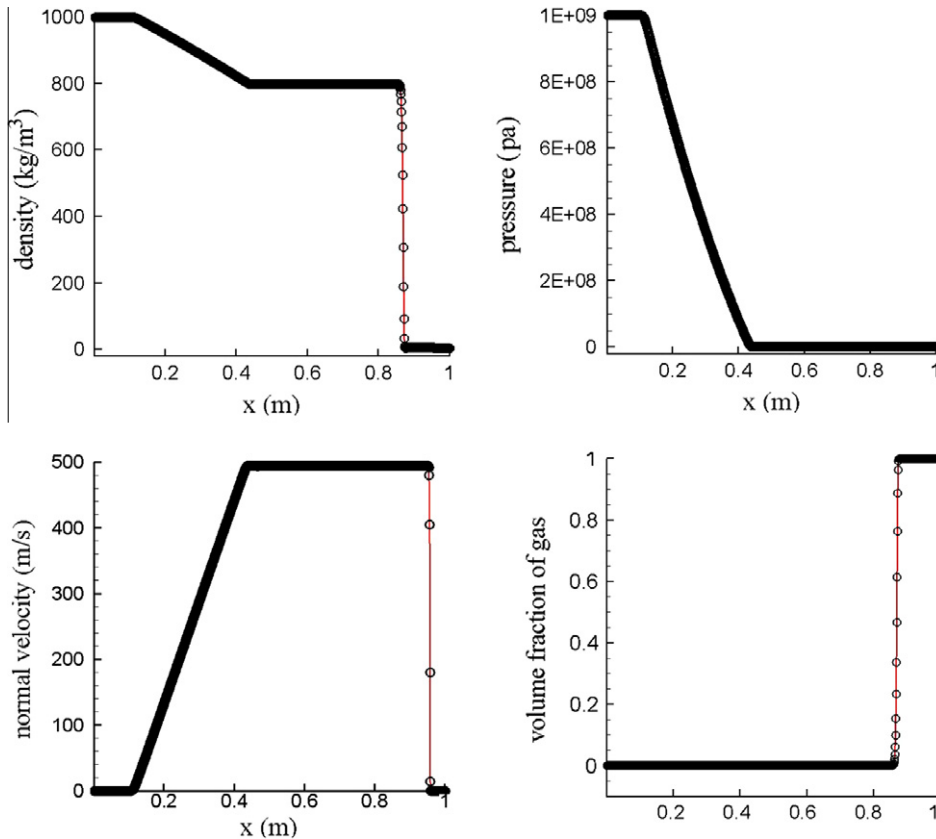


Fig. 3. Comparison of numerical schemes (symbols) and the exact solution (solid lines) for the liquid–gas shock tube, 1000 computational cells, CFL = 0.8.

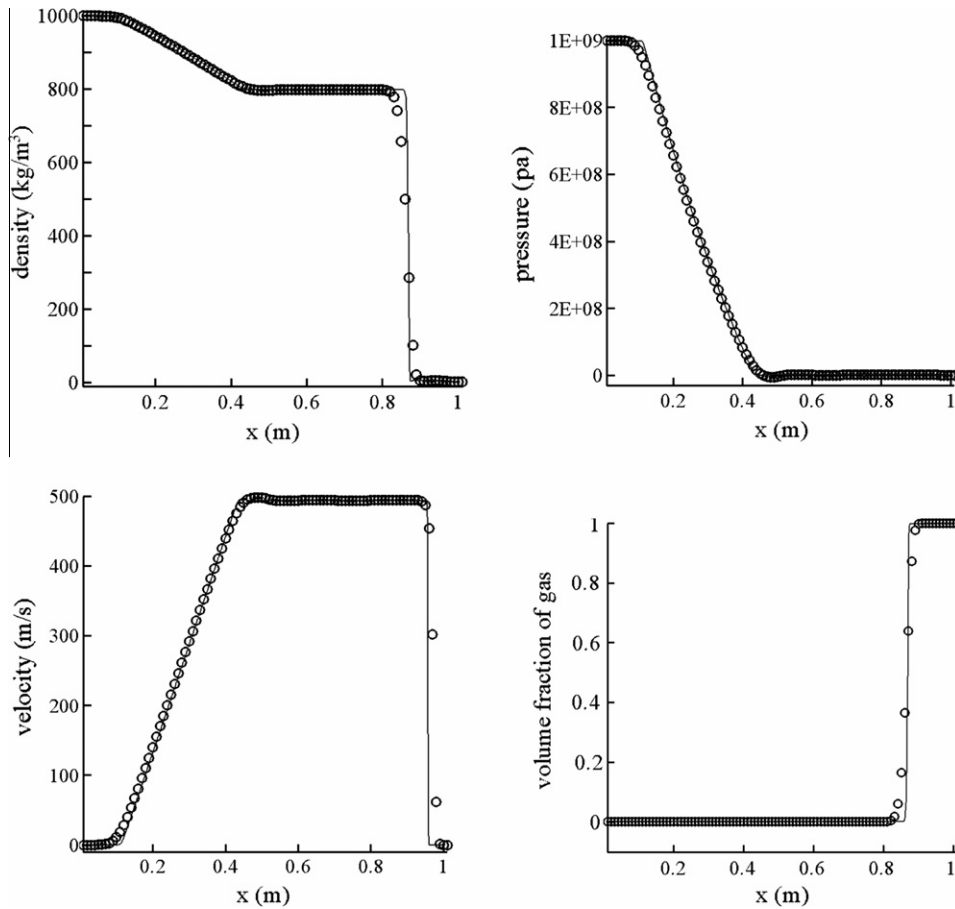


Fig. 4. Comparison of numerical schemes (symbols) and the exact solution (solid lines) for the liquid-gas shock tube. 100 computational cells, CFL = 0.8.

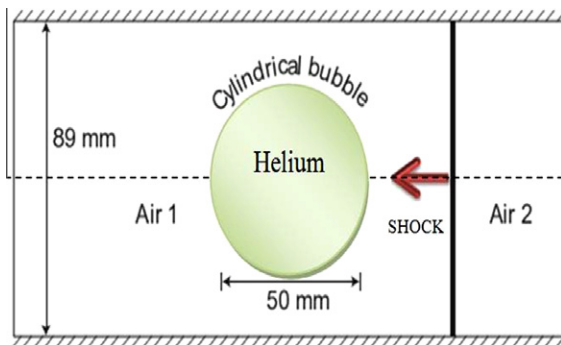


Fig. 5. Initial situation and computational-field configuration for the shock wave and air/helium bubble interaction.

Table 3

Gas properties and initial condition for the test case of interaction between a shock wave and a helium bubble.

	γ	ρ (kg/m ³)	u (m/s)	v (m/s)	P (Pa)	P_{∞} (Pa)
Air 1	1.4	1.4	0.0	0.0	100,000	0
Air 2	1.4	1.92691	-114.42	0.0	156,980	0
Helium	1.648	0.25463	0.0	0.0	100,000	0

results obtained by the numerical method with 200 grids and the analytical solution from Saurel et al. (2009) is good, and there is not any oscillation in the solution.

6.2. Water–air shock tube

This test case considers a shock tube where the left side is filled with high-pressure liquid, and the right side is filled with air. This test case has an exact solution. Each fluid is determined by its stiffened equation of state. The initial condition is defined by Table 2. It should be mentioned that, to the best of our knowledge, all researchers in the published literature used an air density of 50 kg/m³ except for Saurel et al. (2009). In the present study, the initial condition of Saurel et al. (2009) was used, which is a more difficult condition to simulate to demonstrate the high capability of the model when dealing with low pressures. The five-equation model result obtained by numerical solution is compared with the exact solution of the Euler equation in Figs. 3 and 4. Fig. 3 presents results with mesh consists of 1000 uniform computational cells and Fig. 4 uses mesh consists of 100 uniform computational cells. Comparison of numerical results and analytical results are presented at 240 μ s. In this test case, strong pressure waves are propagated. The obtained results are stable and the agreement between the results of both methods is very good. This implies that the model is very capable and the solution method is accurate.

6.3. Two-dimensional test cases

6.3.1. Two-dimensional interaction of shock and air/helium bubble

In this section, the practical case of the interaction between a shock wave and a helium bubble is examined. The experimental

test case are provided in Table 1. The numerical solution at $t = 2.79$ ms is presented in Fig. 2. The agreement between the

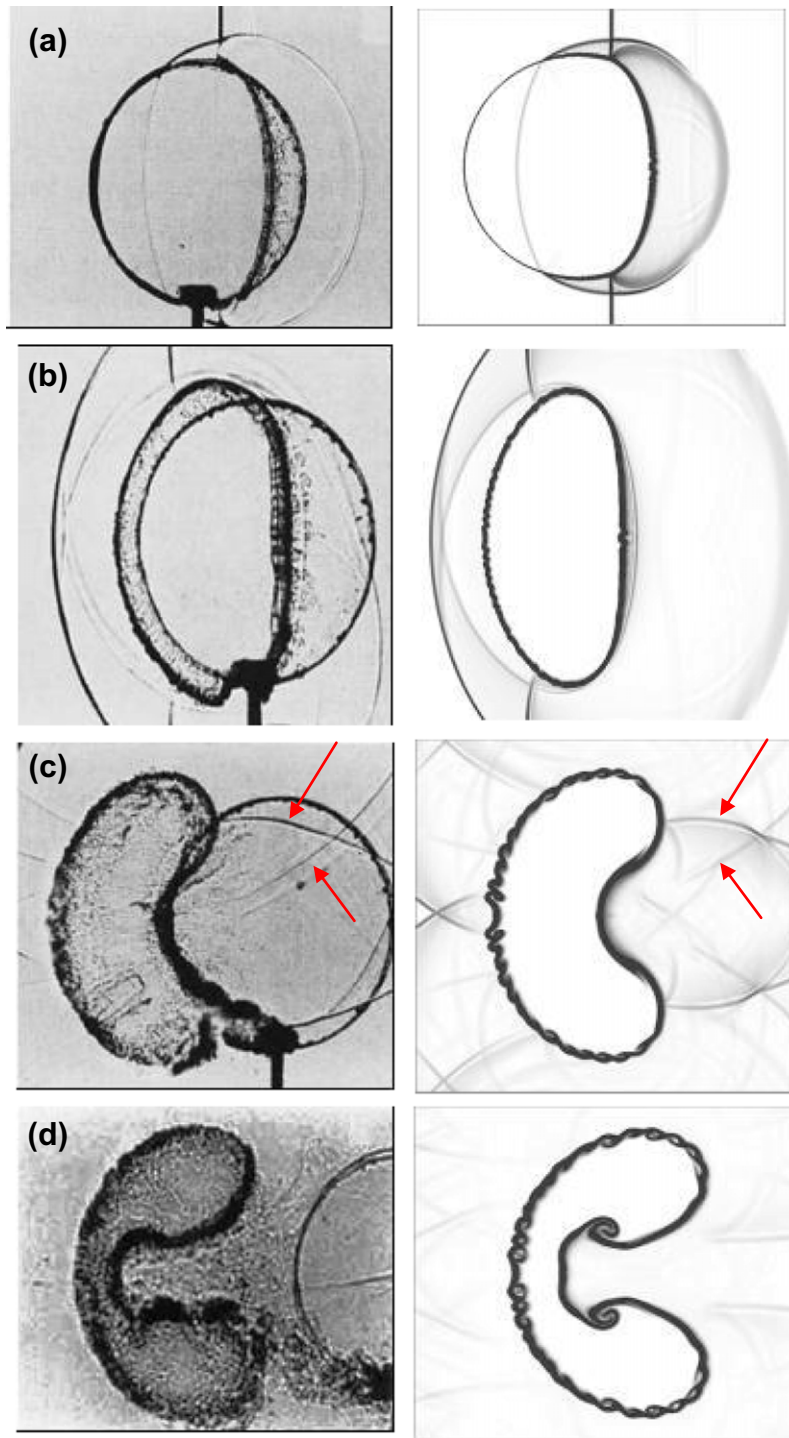


Fig. 6. Shock and air/helium bubble interaction. Left: shadow-photographs of Haas and Sturtevant (1987), right: Numerical Schlieren-type results at: (a) $t = 52 \mu\text{s}$, (b) $t = 102 \mu\text{s}$, (c) $t = 245 \mu\text{s}$ and (d) $427 \mu\text{s}$.

result of this case has been obtained by Haas and Sturtevant (1987). This case is an excellent benchmark for comparison of numerical result accuracy and it has been widely used by researchers to check the accuracy and capability of their numerical methods (Quirk and Karni, 1996; Terashima and Tryggvason, 2009, 2010; Johnsen and Colonius, 2006; Kreeft and Koren, 2010; Qamar and Ahmed, 2009; Kokh and Lagoutière, 2010). In this test case, a plane shock wave with $M_s = 1.22$ is moving in air and hits a cylindrical helium bubble. During the experiments, bubbles are produced by inflating a cylindrical former with very thin walls made

of a nitrocellulose membrane. As the shock wave impacts bubble, the one-dimensional structure of the shock wave is deformed and the bubble loses its circular shape. Interesting consecutive pictures showing the shock wave transition from the bubble have been obtained by Haas and Sturtevant (1987). Fig. 5 shows the schematic flow-field solution of this problem. Dimensions of spatial computational domain are $267 \times 89 \text{ mm}^2$. The initial condition of the case is given in Table 3. The numerical results were obtained by mesh consists of 400×1200 uniform computational cell with CFL = 0.8.

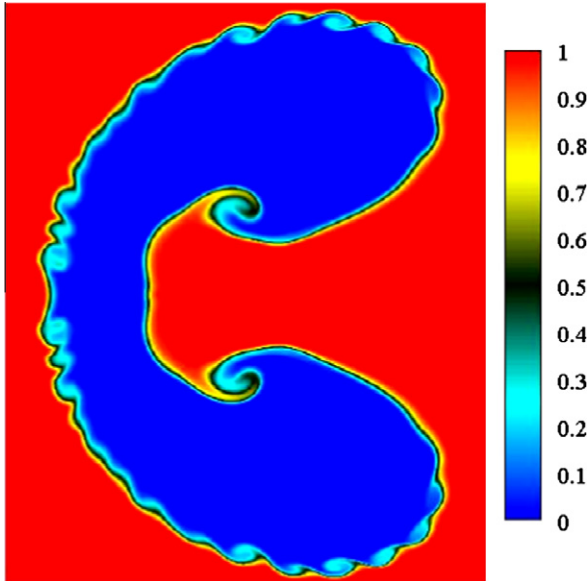


Fig. 7. Enlarged view of the interface topology at 432 μ s, with instabilities occurring at the interface, for a Mach 1.22 shock interacting with a helium cylindrical bubble.

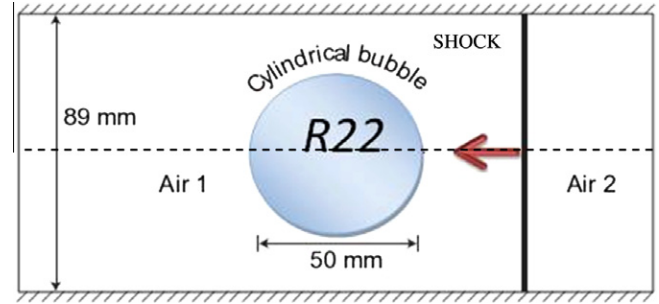


Fig. 9. Initial situation and computational field configuration for the shock wave and air/R22 bubble interaction.

Table 4

Gas properties and initial condition for the interaction between a shock wave and an R22 bubble.

	γ	ρ (kg/m ³)	u (m/s)	v (m/s)	P (Pa)	P_{∞} (Pa)
Air 1	1.4	1.4	0.0	0.0	100,000	0
Air 2	1.4	1.92691	−114.42	0.0	156,980	0
R22	1.249	4.41540	0.0	0.0	100,000	0

Fig. 6 shows the Schlieren-type numerical solution on the right side and the experimental results on the left side (Haas and Sturtevant, 1987). The shock wave moves from right to left. As the sound velocity in the helium inside the bubble is higher than the sound velocity in the air surrounding the bubble, the transmitted shock wave inside bubble moves (propagates) in front of the impacted shock wave. As can be seen from Fig. 6 at 52 μ s, the shock wave reaches almost to the end of the bubble. There is also a reflected shock wave that is created by the interaction that occurred at the initial impact with the bubble, and this shock wave moves backwards. Because of the circular shape of the bubble, the refracted shock wave also has a curved shape. For the same reason,

the reflected shock waves and transmitted shock waves are curved in shape. Fig. 6b shows the interaction of the shock wave and the bubble just a short time before the shock wave leaves the bubble. Fig. 6c clearly shows a ripple-like structure of reflected shock waves from the top and bottom walls. A jet flow from the surrounding air is injected into the bubble from the upstream air. At 427 μ s, the jet is more clearly visible and the vorticity has increased considerably. As can be seen from Fig. 6c and d, the Kelvin–Helmholtz instability is generated by velocity shear and the differences in density at the interface. This instability has been previously captured by a few numerical methods (Johnsen and Colonius, 2006; Marquina and Mulet, 2003), which are more

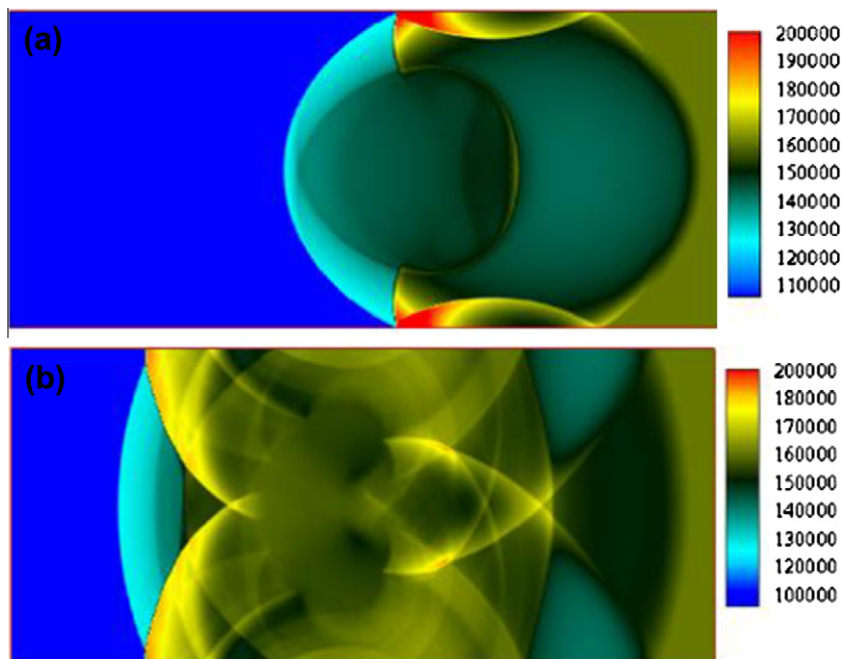


Fig. 8. Contours of the pressure distribution for the shock wave and air/helium interaction at: (a) $t = 102 \mu$ s and (b) $t = 245 \mu$ s.

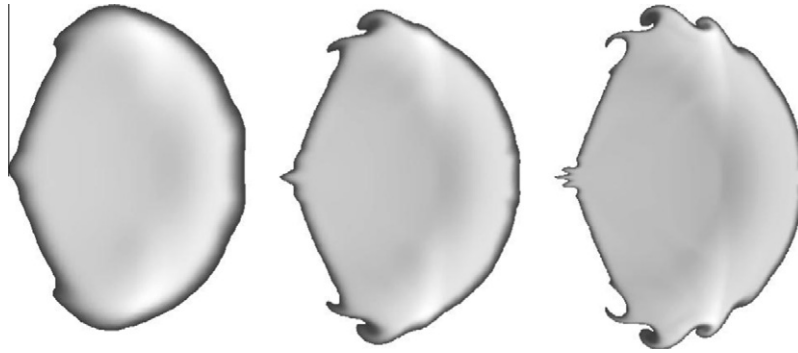


Fig. 10. Grid refinement test (left: 200×100 , middle: 400×200 , right: 800×400).

complicated methods. To present a clear picture of this instability at the interface, the contours of the volume fraction variation are shown in Fig. 7.

As can be seen, even though the method presented here is based on diffusion at the interface, the generated diffusion at the interface is very low and is comparable with sharp interface (SIM) methods. Fig. 8 shows the pressure distribution in the flow field.

Because the sound velocity in the helium bubble is higher than the sound velocity of the surroundings, the helium bubble acts as a concave lens for the incident shock wave. This feature has been pointed out in Banks et al. (2007).

In contrast to the present situation, an opposite condition is formed for an R22 bubble where the sound velocity in R22 bubbles is lower than the air sound velocity, and the bubble acts as a

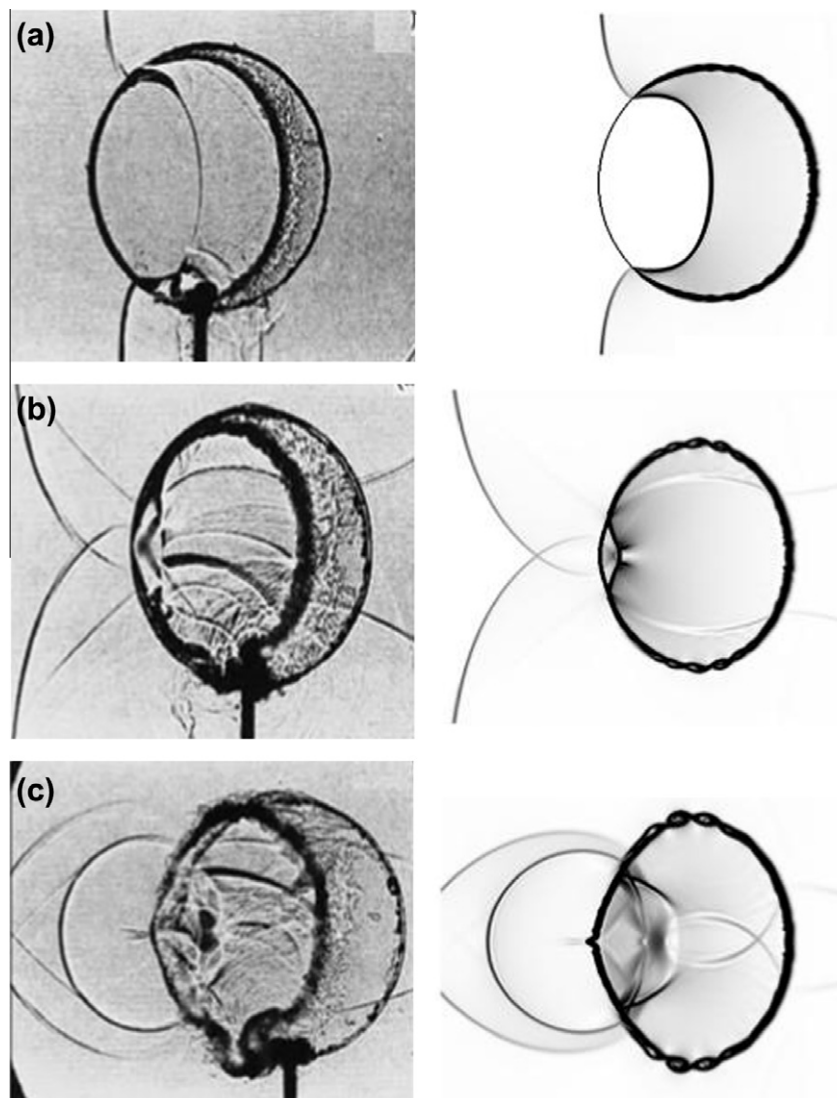


Fig. 11. Shock wave and air/R22 bubble interaction. Left: shadow-photographs of Haas and Sturtevant (1987), right: Numerical Schlieren-type results at: (a) $t = 115 \mu\text{s}$, (b) $t = 187 \mu\text{s}$ and (c) $t = 247 \mu\text{s}$.

concave lens for the incident shock wave. This example can be seen more clearly in the pressure contours of Fig. 8. This figure also shows the reflected wave formed due to hitting the incident shock wave with the wall, which has strong pressure waves towards the center of channel. The propagation velocity of these waves to the front is higher than the velocity of the transmitted shock wave.

6.3.2. Two-dimensional interaction of shock wave and bubble, air/R22

Two-dimensional shock wave and R22 bubble interaction is demonstrated. The experimental result of this test case has been conducted by Haas and Sturtevant (1987) to provide a reliable benchmark. Similar to the previous test case, which can be used for comparison of the accuracy of numerical simulation results, this test case has been used for comparison by many researchers (Quirk and Karni, 1996; Kreeft and Koren, 2010; Qamar and Ahmed, 2009; Kokh and Lagoutière, 2010; Banks et al., 2007; Nourgaliev et al., 2006; Sambasivan and UdayKumar, 2010). In this test case, a planar shock wave is moving in the air with $M_s = 1.22$ and collides with a cylindrical R22 bubble. The main difference between this problem and the previous case of the helium bubble is that the sound velocity in helium is greater than that of air, and for an R22 bubble, the reverse is true. Fig. 9 shows the schematic solution-field of the test case. The flow-field dimensions are 178×89 mm. The initial condition of the case is presented in Table 4. Fig. 10 shows the R22 bubble shape computed on the three grids at time = 383 μ s. Overall, the evolution of the bubble shape is similar on the three grids numbers, despite the large interface deformation. With the higher grid refinement the shear instability on the fluid interface is enhanced.

Fig. 11 shows a sequence of experimental shadow images and the corresponding computational Schlieren-type images. The total number of cells is 400×800 , and the CFL = 0.8. The Schlieren-type image is created with the nonlinear shading function used in Quirk and Karni (1996) in order to heighten weak flow features. R22 has a higher density and a lower ratio of specific heats than air, resulting in a speed of sound about two times lower than that of air. The lower speed of sound causes the shock wave inside the bubble, the refracted shock wave, to be delayed behind the incoming shock (Fig. 11). Furthermore, the velocity of air behind the incident shock wave is greater than the velocity of air behind the transmitted shock wave inside the bubble. This velocity difference introduces a counter-clockwise shear tension on the surface of the bubble, which later leads to Kelvin–Helmholtz (K–H) instability. In addition, the accelerated contact surface is deformed, and Richtmyer–Meshkov (R–M) instability is observed due to the interaction of the shock system with the curved front of the bubble. The unstable interface eventually rolls up to form vortices and fragments of vortices on the interface. For a more visible presentation of these instabilities, Fig. 12 is presented for the volume fraction changes. The difference between the K–H instability in R22 bubble and that of the helium bubble of Fig. 7 is that the rolled-up vortical structure of the helium bubble occurs towards the inside of the bubble; however, in the R22 case, the rolled-up vortical structure is formed towards the outside of the bubble. The results obtained from the numerical simulation exhibit no oscillation and have enough resolution to simulate the Richtmyer–Meshkov (R–M) and Kelvin–Helmholtz (K–H) instabilities. For more validation of the present algorithm a direct qualitative comparison of our results is made with the existing numerical results that obtained by previous investigators, see Fig. 13. The present method is comparable to results of both methods of adaptive mesh refinement (AMR) (Banks et al., 2007; Nourgaliev et al., 2006) and local mesh refinement (LMR) (Sambasivan and UdayKumar, 2010; Reimann et al., 2009). These methods are more complicated in comparison to the present method, and the present results are in good agreement with them.

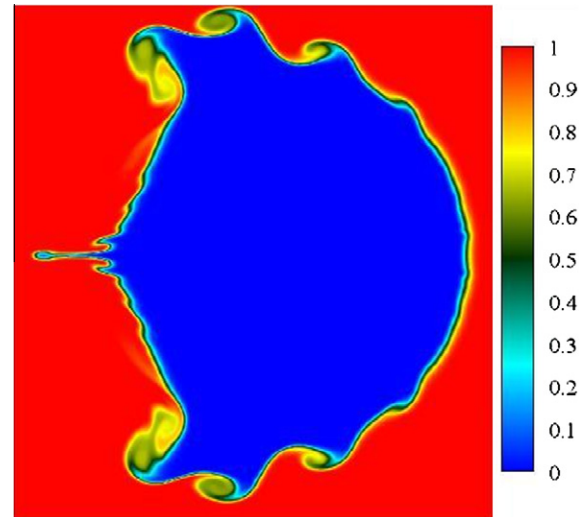


Fig. 12. Enlarged view of the interface topology at 432 μ s, instabilities occurring at the interface, for a Mach 1.22 shock interacting with R22 cylindrical bubble.

The present method has not only high accuracy in comparison to other methods, but it is also very simple. As has been discussed in Nourgaliev et al. (2006), the other LMR numerical methods can capture K–H and R–M instabilities only when a high number of mesh cells are used at the interfaces. Fig. 14 shows the pressure distribution in the flow field. It shows re-reflected pressure waves that have collided with the wall as well as interaction with other pressure waves. The results of our simulations are in sensitive agreement with the experimental data, resolving the general shape of the bubble, the complex shock wave refraction patterns, the formation of vorticities due to Richtmyer–Meshkov (R–M) and Kelvin–Helmholtz (K–H) instabilities and the R22 jet.

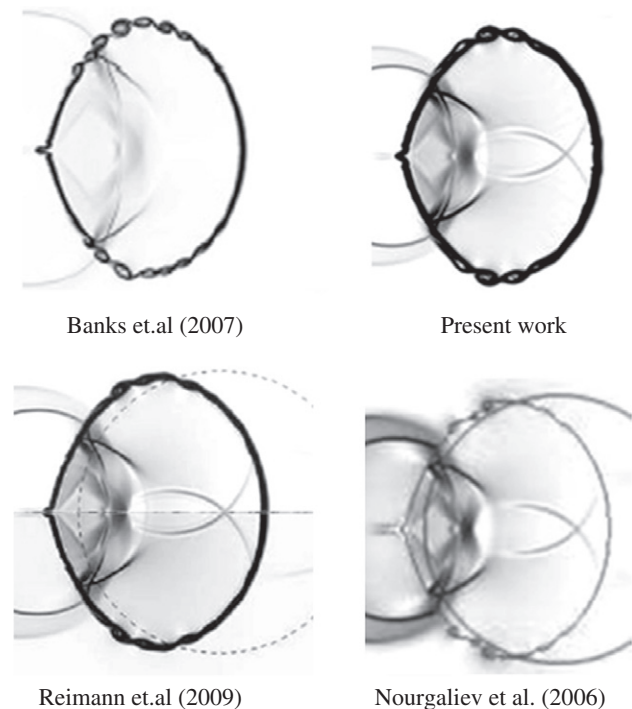


Fig. 13. Qualitative comparison between present numerical result and previous results of some sharp interface methods by other researchers. Shock and R22 bubble interaction at 247 μ s.

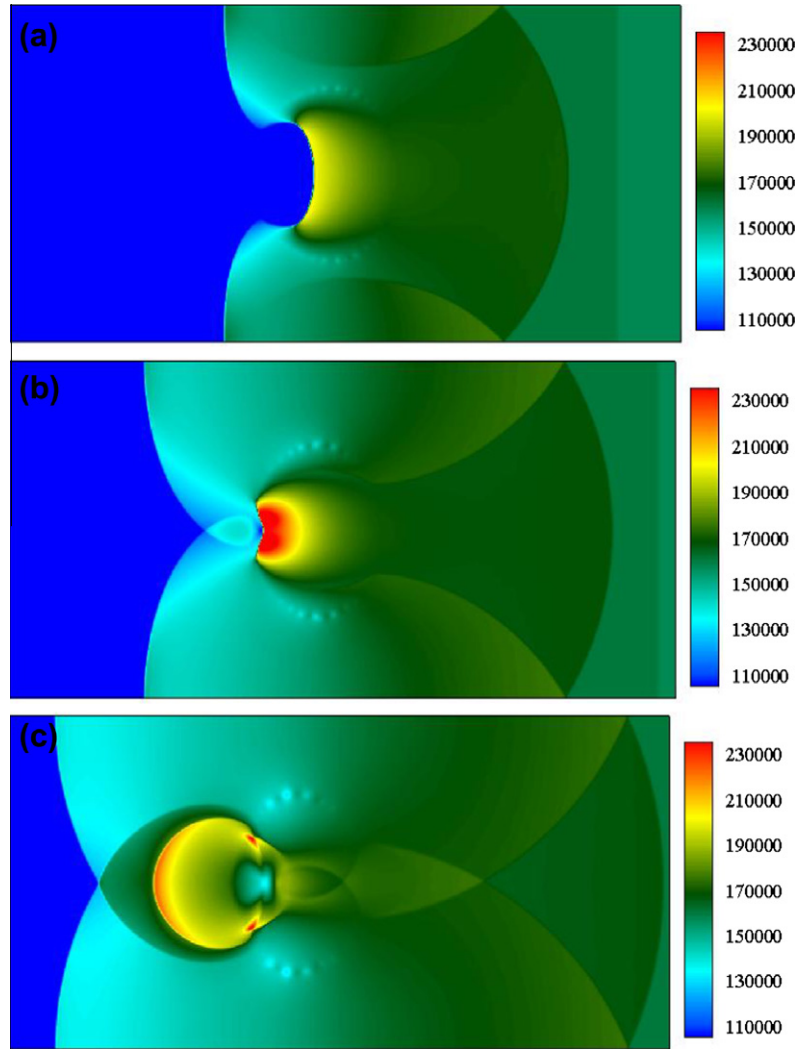


Fig. 14. Contours of the pressure distribution of the shock wave and air/R22 bubble interaction (CFL = 0.8) for: (a) $t = 115 \mu\text{s}$, (b) $t = 187 \mu\text{s}$ and (c) $t = 247 \mu\text{s}$.

6.3.3. Interaction of a shock wave colliding with an air bubble in water

This test case is considered a complicated problem because of the large difference in the densities of the two phases of air and water and the effects of interaction between the shock wave and the bubble. This test case is commonly used for testing numerical methods. For this test case, a cylindrical bubble with a 6 mm diameter is assumed inside of a water pool. The bubble is collapsed by a shock wave moving at Mach 1.72. The solution flow-field is a rectangle with dimensions of $24 \times 29 \text{ mm}$ and with the center of bubble positioned at (12, 12) mm. The shock wave begins 16 mm from the center of bubble on the right side. The initial condition of this test case is shown in Table 5.

The top and bottom boundary conditions are assumed to be walls, and the boundary conditions for the left and right sides are assumed to be non-reflecting (Toro, 1999). The schematic diagram of the test case is given in Fig. 15. The numerical solution is

conducted with 360,000 mesh cells. The time evaluation of the simulation results is presented in Fig. 16 in the Schlieren-type representation. Figs. 17 and 18 show the pressure distribution contours and the volume fraction distribution. After the water shock wave has collided with the bubble, a strong rarefaction wave is reflected backwards from the interface, and a weak shock wave transmits from inside of the bubble. This weak shock wave is visible only in the Schlieren-type presentation of Fig. 16a. A water jet

Table 5

Initial condition for the effect of shock wave and air bubble interaction in water.

	γ	$\rho \text{ (kg/m}^3\text{)}$	$u \text{ (m/s)}$	$v \text{ (m/s)}$	$P \text{ (Pa)}$	$P_\infty \text{ (Pa)}$
Water 1	4.4	1000	0.0	0.0	1.0×10^5	6e8
Water 2	4.4	1323.65	-681.58	0.0	1.9×10^9	6e8
Air	1.4	1	0.0	0.0	1.0×10^5	0.0

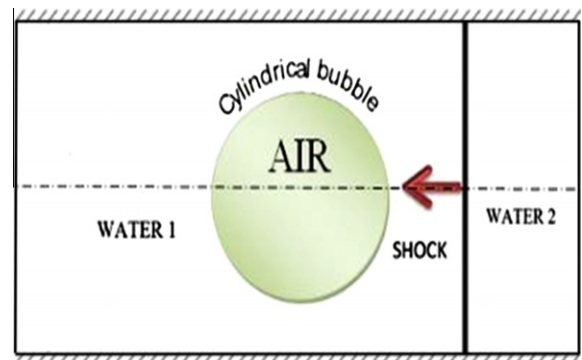


Fig. 15. Schematic of the initial flow field and the computational domain.

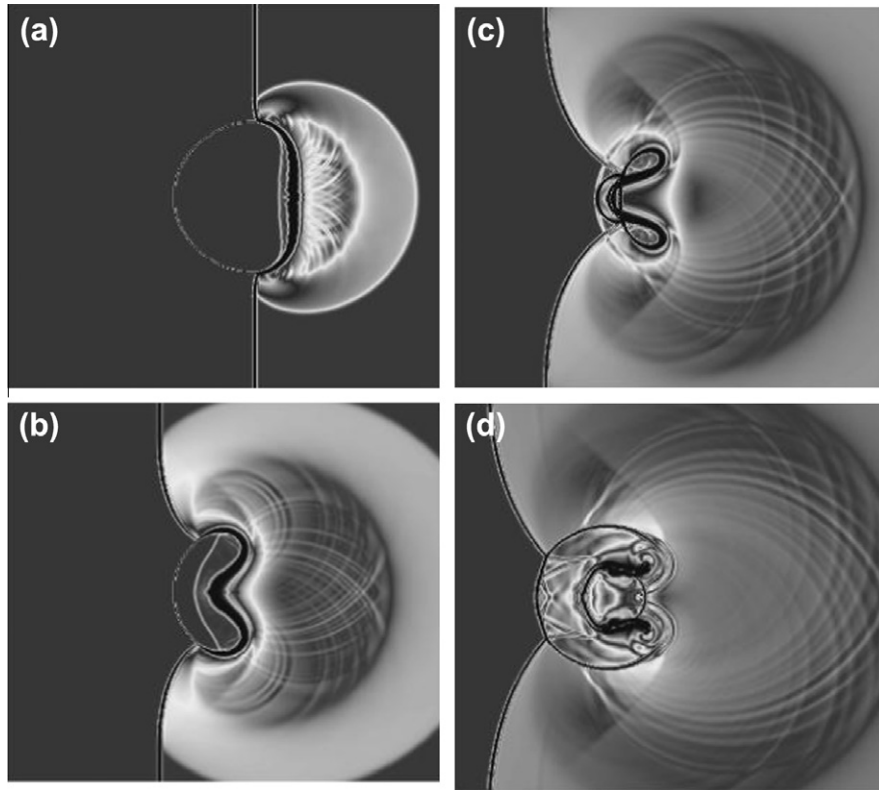


Fig. 16. Numerical Schlieren-type results of the shock wave and water/air bubble interaction (CFL = 0.8) at: (a) $t = 5.8 \mu\text{s}$, (b) $t = 7.0 \mu\text{s}$, (c) $t = 7.75 \mu\text{s}$ and (d) $t = 8.5 \mu\text{s}$.

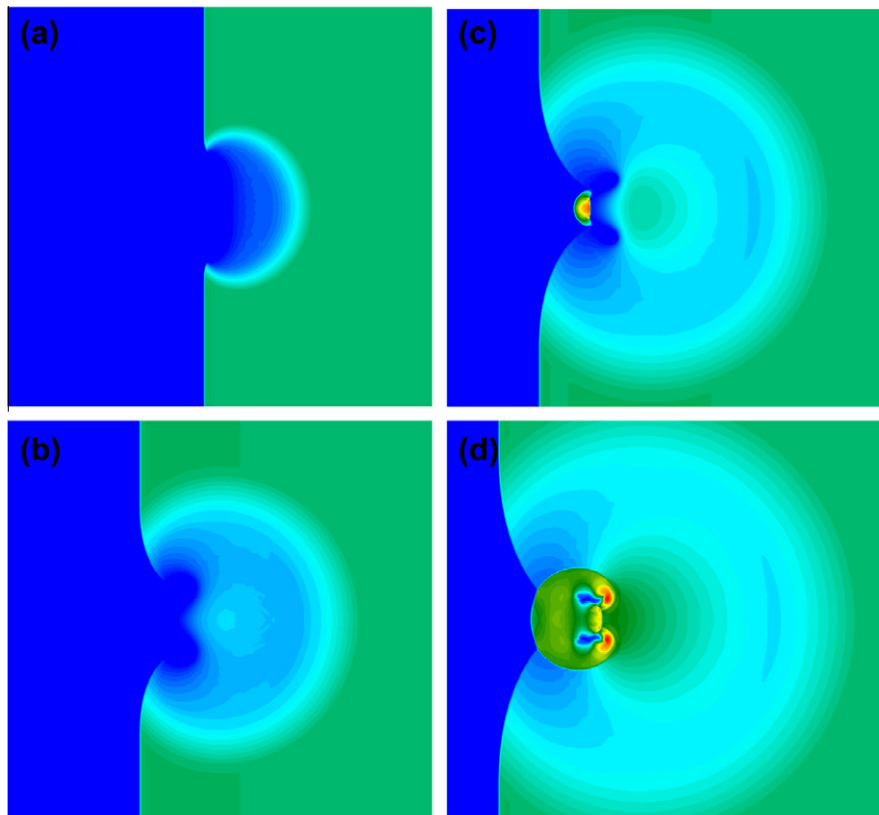


Fig. 17. Contours of the pressure distribution for the shock wave and water/air interaction (CFL = 0.8) at: (a) $t = 5.8 \mu\text{s}$, (b) $t = 7.0 \mu\text{s}$, (c) $t = 7.75 \mu\text{s}$ and (d) $t = 8.5 \mu\text{s}$.

is formed by the rarefaction wave, which pushes the bubble along the centerline direction to bend the bubble into a crescent shape

(arc). Finally, the bubble is divided into two sections as a result of the water jet, each section becomes a bubble, and the water

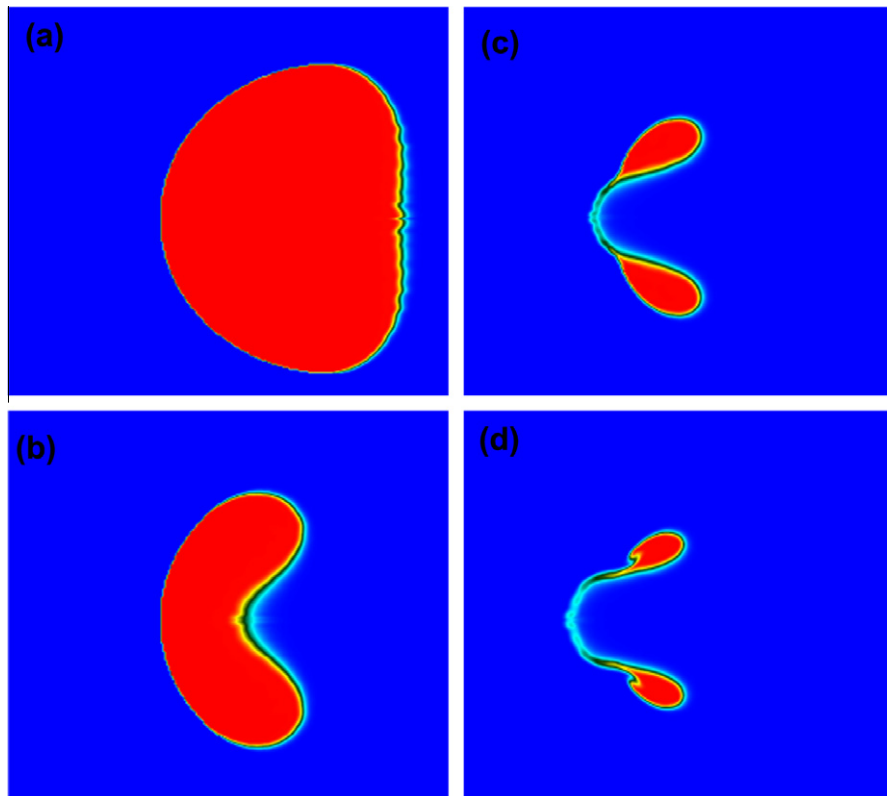


Fig. 18. Time evolution of the volume fraction for the shock wave and water/air bubble interaction (CFL = 0.8) at: (a) $t = 5.8 \mu\text{s}$, (b) $t = 7.0 \mu\text{s}$, (c) $t = 7.75 \mu\text{s}$ and (d) $t = 8 \mu\text{s}$.

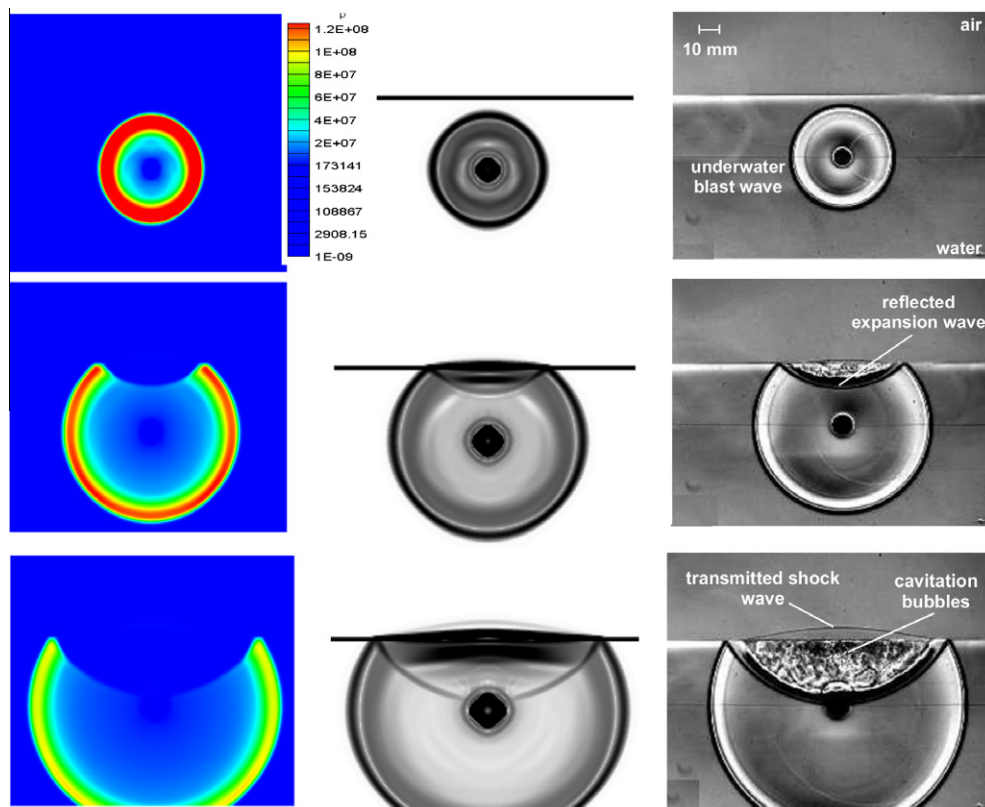


Fig. 19. Wave structure of underwater explosion of AgN₃. Left column shows the pressure contours of numerical results. Middle column shows the patterns of Schlieren-type images obtained in present numerical simulations. Right column shows experimental shadowgraph photographs by Kleine et al. (2009). From top to below: 14 μs , 28 μs , 42 μs .

jet hits the stationary water at the front of the bubble with very high velocity. During the impact of the water jet with the stationary water at the front of the bubble, a high-pressure zone is formed, and a shock wave is generated. Fig. 17 shows that this shock wave expands continuously in the radial direction. Reflected waves from the walls are also formed by different waves interacting with the wall. These generated reflected waves have complicated interactions with the bubble and the flow field. As time increases, the air bubble becomes smaller and smaller (shrinks) and eventually disappears. Time evolution of the volume fraction and the topology of the bubble interface are shown in Fig. 18. The results obtained show no numerical oscillation and have good agreement with previous research results (Wang and Shu, 2010; Nourgaliev et al., 2006; Shukla et al., 2010).

6.3.4. Free-surface underwater explosion of AgN3

In this section an underwater explosion problem is considered. The phenomena involved in this test case recently have been studied experimentally by Kleine et al. (2009). In this problem, the explosion of 10 mg silver Azide (AgN₃) modeled as a sphere core with a diameter of 1 cm, which releases energy of 25.5 J/m. To attain the initial condition of this problem, the experimental data provided by Kleine et al. (2009) is used. The initial pressure in the explosive core is set to approximately to 10^9 Pa. The gravitational force and hydrostatic pressure effects are considered. At $t = 0$, the fluids are at rest in the whole domain. The computational field is a square domain of 0.35×0.35 m². At $t = 0$, the free surface is at $y = 0.175$ m. The explosive as a pressurized liquid circular core is located at 0.05 m below the free surface. The bottom boundary is solid wall, while transparent boundaries condition is imposed for the top, left and right domain boundaries. The domain is discretized with 300×300 grids.

Fig. 19 presents comparison of Schlieren-type images of density by numerical methods of present work and experimental investigation by Kleine et al. (2009). There is a good qualitatively concurrence between the simulated results and experimental data. The profiles of the pressure at the instants of $t = 14, 28, 42$ μ s are also displayed in Fig. 19. After the explosion initiation, the main shock expands radially outwards into the water. The main shock impacts the free-surface, causing formation of the reflected Prandtl–Meyer rarefaction wave, and a weak transmitted air shock. The tension waves caused by the reflected shock from free surface are responsible mechanism for the formation of the observed cavitation near and below the free surface.

7. Concluding remarks

A simple methodology based on the Godunov numerical method and the HLLC Riemann solver is applied with second-order accuracy to simulate compressible transient one- and two-dimensional two-phase flows in the presence of a shock wave. Modeling of strong rarefaction waves as cavitations is accomplished by coupling the Schmidt cavitation model to the five-equation Kapila model. This numerical method, which is a subset of the diffuse interface method, uses a constant computational grid that is simple and easy to apply. The capability and effectiveness of the numerical method were investigated for different two-phase gas–gas and gas–liquid flows in the present of shock wave and for flows with strong rarefaction cavitations waves.

The numerical results for 1D and 2D simulations were accurate with no numerical oscillation. These results are in good agreement with experimental results and previous numerical results obtained by more sophisticated numerical methods. The present numerical method can quite accurately capture R–M and K–H instabilities at an interface during mutual interaction of a shock wave and an

air/helium or air/R22 bubble. The accuracy of the present method for obtaining interfacial instabilities compares well with more complicated numerical methods such as AMR and LMR. The other advantage of using this method is that there is no need to decrease the CFL value or to create a very fine mesh for most of the problems, which reduces the computation time considerably. Finally, it can be declared that the present numerical method has the capability and effectiveness of simulating many two-phase gas–gas and gas–liquid flow test cases in the present of shock waves and test cases with strong rarefaction waves similar to cavitations flows.

References

- Abgrall, R., 1996. How to prevent pressure oscillations in multi component flow calculations: a quasi conservative approach. *J. Comput. Phys.* 125 (1), 150–160.
- Anbarlooei, H.R., Mazaheri, K., 2009. Moment of fluid interface reconstruction method in multi-material arbitrary Lagrangian Eulerian (MMALE) algorithms. *Comput. Meth. Appl. Mech. Eng.* 198, 3782–3794.
- Baer, M., Nunziato, J., 1986. A two-phase mixture theory for the deflagration-to-detonation transition (DDT) in reactive granular materials. *Int. J. Multiphase Flows* 12, 861–889.
- Banks, J.W. et al., 2007. A high-resolution Godunov method for compressible multi-material flow on overlapping grids. *J. Comput. Phys.* 223, 262–297.
- Chang, C.-H., Liou, M.-S., 2007. A robust and accurate approach to computing compressible multiphase flow: stratified flow model and AUSM +up scheme. *J. Comput. Phys.* 225, 840–873.
- Davis, S.F., 1998. Simplified second-order Godunov-type methods. *SIAM J. Sci. Statist. Comput.* 9, 445–473.
- Deledicque, V., Papalexandris, M.V., 2007. An exact Riemann solver for compressible two-phase flow models containing non-conservative products. *J. Comput. Phys.* 222, 217–245.
- Doneal, J., Huerta, A., Ponthot, J.P., Rodriguez-Ferran, A., 2004. Arbitrary Lagrangian–Eulerian methods. In: Stein, E., de Borst, R., Hughes, T.J. (Eds.), *Encyclopedia of Computational Mechanics*. John Wiley & Sons (Chapter 14).
- Dumbser, M., Toro, E.F., 2010. A simple extension of the Osher Riemann solver to non-conservative hyperbolic systems. *J. Sci. Comput.* <http://dx.doi.org/10.1007/s10915-010-9400-3>.
- Haas, J.F., Sturtevant, B., 1987. Interaction of weak shock waves with cylindrical and spherical gas in homogeneities. *J. Fluid Mech.* 181, 41–76.
- Hu, X.Y. et al., 2009. On the HLLC Riemann solver for interface interaction in compressible multi-fluid flow. *J. Comput. Phys.* 228, 6572–6589.
- Johnsen, E., Colonius, T., 2006. Implementation of WENO schemes in compressible multi component flow problems. *J. Comput. Phys.* 219, 715–732.
- Kapila, Menikoff, R., Bdzil, J., Son, S., Stewart, D., 2001. Two-phase modeling of DDT in granular materials: reduced equations. *Phys. Fluid* 13, 3002–3024.
- Kawai, S., Terashima, H., 2010. A high-resolution scheme for compressible multi component flows with shock waves. *Int. J. Numer. Meth. Fluids*.
- Kleine, H., Tepper, S., Takehara, K., Etoh, T.G., Hiraki, K., 2009. Cavitation induced by low-speed underwater impact. *Int. J. Shock Waves* 19, 895.
- Kokh, S., Lagoutière, F., 2010. An anti-diffusive numerical scheme for the simulation of interfaces between compressible fluids by means of a five-equation model. *J. Comput. Phys.* 229, 2773–2809.
- Kreeft, J.J., Koren, B., 2010. A new formulation of Kapila's five-equation model for compressible two-fluid flow, and its numerical treatment. *J. Comput. Phys.* 229, 6220–6242.
- Marquina, P., Mulet, A., 2003. Flux-split algorithm applied to conservative models for multi component compressible flows. *J. Comput. Phys.* 185, 120–138.
- Munkejord, S.T., 2010. A numerical study of two-fluid models with pressure and velocity relaxation. *Adv. Appl. Math. Mech.* 2, 131–159.
- Murrone, A., Guillard, H., 2005. A five-equation reduced model for compressible two-phase flow problems. *J. Comput. Phys.* 202 (2), 664–698.
- Nourgaliev, R.R., Dinh, T.N., Theofanous, T.G., 2006. Adaptive characteristics-based matching for compressible multi fluid dynamics. *J. Comput. Phys.* 213, 500–529.
- Osher, S., Fedkiw, R., 2001. Level set methods: an overview and some recent results. *J. Comput. Phys.* 169 (2), 463–502.
- Petitpas, F., Franquet, E., Saurel, R., Le Metayer, O., 2007. A relaxation-projection method for compressible flows. Part II: Artificial heat exchanges for multiphase shocks. *J. Comput. Phys.* 225 (2), 2214–2248.
- Petitpas, F., Saurel, R., Franquet, E., Chinnayya, A., 2009. Modeling detonation waves in condensed materials: multiphase CJ conditions and multidimensional computations. *Shock Waves* 19, 377–401.
- Pilliod, J., Puckett, E., 2004. Second-order accurate volume-of-fluid algorithms for tracking material interfaces. *J. Comput. Phys.* 199, 465–502.
- Qamar, S., Ahmed, M., 2009. A high order kinetic flux-vector splitting method for the reduced five-equation model of compressible two-fluid flows. *J. Comput. Phys.* 228, 9059–9078.
- Quan, S., Schmidt, D.P., 2007. A moving mesh interface tracking method for 3D incompressible two-phase flows. *J. Comput. Phys.* 221, 761–780.
- Quirk, J.J., Karni, S., 1996. On the dynamics of a shock-bubble interaction. *J. Fluid Mech.* 318, 129–163.
- Reimann, B., Hannemann, V., Hannemann, V., 2009. computations of shock wave propagation with local mesh adaption. *Shock Waves Part XX*, 1383–1388.

- Sambasivan, S.K., UdayKumar, H.S., 2010. Sharp interface simulations with Local Mesh Refinement for multi-material dynamics in strongly shocked flows. *Comput. Fluids* 39, 1456–1479.
- Saurel, R., Abgrall, R., 1999. A multiphase Godunov method for compressible multi fluid and multiphase flows. *J. Comput. Phys.* 150 (2), 425–467.
- Saurel, R., Le Metayer, O., 2001. A multiphase model for interfaces, shocks, detonation waves and cavitation. *J. Fluid Mech.* 431, 239–271.
- Saurel, R., Franquet, E., Daniel, E., Le Metayer, O., 2007. A relaxation-projection method for compressible flows. Part I: The numerical equation of state for the Euler equations. *J. Comput. Phys.* 223 (2), 822–845.
- Saurel, R., Petitpas, F., Berry, R.A., 2009. Simple and efficient relaxation methods for interfaces separating compressible fluids, cavitating flows and shocks in multiphase mixtures. *J. Comput. Phys.* 228 (5), 1678–1712.
- Schmidt, D.P., 1997. Cavitation in Diesel Fuel Injector Nozzles. PhD Thesis, Wisconsin, University.
- Sethian, J.A., 1996. Level Set Methods: Evolving Interfaces in Geometry, Fluid. Mechanics, Computer Vision and Material Science. Cambridge University Press.
- Shopov, P.J., Minev, P.D., Bazhekov, I.B., Zapryanov, Z.D., 1990. Interaction of a deformable bubble with a rigid wall at moderate Reynolds numbers. *J. Fluid Mech.* 219, 241–271.
- Shukla, R.K. et al., 2010. An interface capturing method for the simulation of multiphase compressible flows. *J. Comput. Phys.* 229, 7411–7439.
- Shyue, K.-M., 1998. An efficient shock-capturing algorithm for compressible multi component problems. *J. Comput. Phys.* 142, 208–242.
- Shyue, K.-M., 2010. A high-resolution mapped grid algorithm for compressible multiphase flow problems. *J. Comput. Phys.* 229, 8780–8801.
- Terashima, H., Tryggvason, G., 2009. A front-tracking/ghost-fluid method for fluid interfaces in compressible flows. *J. Comput. Phys.* 228, 4012–4037.
- Terashima, H., Tryggvason, G., 2010. A front-tracking method with projected interface conditions for compressible multi-fluid flows. *Comput. Fluids* 39, 1804–1814.
- Tokareva, S.A., Toro, E.F., 2010. HLLC-type Riemann solver for the Baer–Nunziato equations of compressible two-phase flow. *J. Comput. Phys.* 229, 3573–3604.
- Toro, E.F., 1999. *Riemann Solvers and Numerical Methods for Fluid Dynamics*. Springer, Berlin.
- Unverdi, S., Tryggvason, G., 1992. A front tracking method for viscous incompressible flows. *J. Comput. Phys.* 100, 25–37.
- Wang, C., Shu, C.-W., 2010. An interface treating technique for compressible multi-medium flow with Runge–Kutta discontinuous Galerkin method. *J. Comput. Phys.* 229, 8823–8843.
- Wood, 1930. *A Textbook of Sound*. G. Bell & Sons Ltd., London.
- Xie, W.F., Liu, T.G., Khoo, B.C., 2006. Application of a one-fluid model for large scale homogeneous unsteady cavitation: the modified Schmidt model. *Comput. Fluids* 35 (10), 1177–1192.